Cell Reports

Spatial Separation of Mitochondrial Calcium Uptake and Extrusion for Energy-Efficient Mitochondrial Calcium Signaling in the Heart

Graphical Abstract

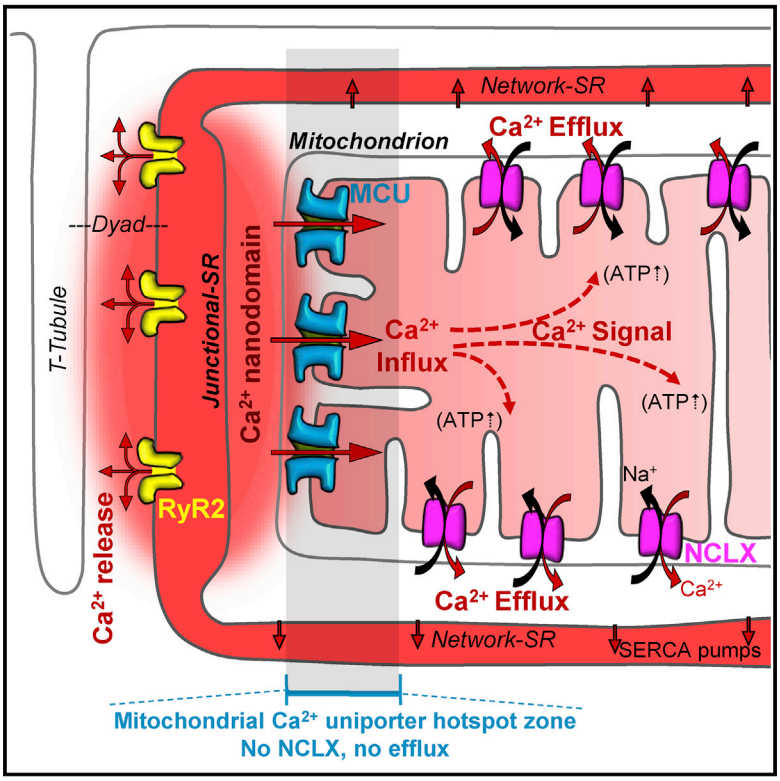

Highlights

- MCU complex (MCUC) and NCLX are spatially separated in heart mitochondria
- Mitochondrial contact with SR Ca^{2+} signal source is an MCUC hotspot but lacks NCLX
- This distribution minimizes the energy cost of maintaining mitochondrial Ca^{2+} signals
- It also optimizes mitochondrial Ca^{2+} signal generation efficacy from Ca^{2+} nanodomains

Authors

Sergio De La Fuente, Jonathan P. Lambert, Zuzana Nichtova, Celia Fernandez Sanz, John W. Elrod, Shey-Shing Sheu, György Csordás

Correspondence

shey-shing.sheu@jefferson.edu (S.-S.S.), gyorgy.csordas@jefferson.edu (G.C.)

In Brief

Calcium signals control mitochondrial fuel generation. De La Fuente et al. report that in heart mitochondria, calcium uptake and extrusion are spatially separated; the most calcium-exposed area is an uptake hotspot, but it lacks extrusion to optimize signaling efficiency and minimize the energy expense of controlling mitochondrial function by calcium.

De La Fuente et al., 2018, Cell Reports *24*, 3099–3107
September 18, 2018
https://doi.org/10.1016/j.celrep.2018.08.040

CellPress

Cell Reports
Report

Spatial Separation of Mitochondrial Calcium Uptake and Extrusion for Energy-Efficient Mitochondrial Calcium Signaling in the Heart

Sergio De La Fuente,[1] Jonathan P. Lambert,[3] Zuzana Nichtova,[1] Celia Fernandez Sanz,[2] John W. Elrod,[3,4] Shey-Shing Sheu,[2,4,*] and György Csordás[1,4,5,*]

[1]MitoCare Center for Mitochondrial Imaging Research and Diagnostics, Department of Pathology, Anatomy, and Cell Biology, Thomas Jefferson University, Philadelphia, PA 19107, USA
[2]Center for Translational Medicine, Department of Medicine, Thomas Jefferson University, Philadelphia, PA 19107, USA
[3]Center for Translational Medicine, Lewis Katz School of Medicine at Temple University, Philadelphia, PA 19140, USA
[4]Senior author
[5]Lead Contact
*Correspondence: shey-shing.sheu@jefferson.edu (S.-S.S.), gyorgy.csordas@jefferson.edu (G.C.)
https://doi.org/10.1016/j.celrep.2018.08.040

SUMMARY

Mitochondrial Ca^{2+} elevations enhance ATP production, but uptake must be balanced by efflux to avoid overload. Uptake is mediated by the mitochondrial Ca^{2+} uniporter channel complex (MCUC), and extrusion is controlled largely by the Na^+/Ca^{2+} exchanger (NCLX), both driven electrogenically by the inner membrane potential ($\Delta\Psi_m$). MCUC forms hotspots at the cardiac mitochondria-junctional SR (jSR) association to locally receive Ca^{2+} signals; however, the distribution of NCLX is unknown. Our fractionation-based assays reveal that extensively jSR-associated mitochondrial segments contain a minor portion of NCLX and lack Na^+-dependent Ca^{2+} extrusion. This pattern is retained upon *in vivo* NCLX overexpression, suggesting extensive targeting to non-jSR-associated submitochondrial domains and functional relevance. In cells with non-polarized MCUC distribution, upon NCLX overexpression the same given increase in matrix Ca^{2+} expends more $\Delta\Psi_m$. Thus, cardiac mitochondrial Ca^{2+} uptake and extrusion are reciprocally polarized, likely to optimize the energy efficiency of local calcium signaling in the beating heart.

INTRODUCTION

Mitochondria play numerous roles in intracellular Ca^{2+} signals as effectors (in energy metabolism and cell death) or as modulators (of cytosolic $[Ca^{2+}]$ ($[Ca^{2+}]_c$) signals). In all of these roles, mitochondrial Ca^{2+} uptake and extrusion are central and must work in a well-coordinated manner. Mitochondrial Ca^{2+} uptake is electrogenic, driven by a large inside negative $\Delta\Psi_m$ (~−180 mV), and mediated primarily by the mitochondrial Ca^{2+} uniporter channel complex (MCUC). MCUC comprises the pore-forming MCU, the essential scaffold EMRE, and the Ca^{2+}-sensing gatekeepers MICU1 and -2 (De Stefani et al., 2016; Kamer and Mootha, 2015; Mammucari et al., 2017; Mishra et al., 2017). The main mitochondrial Ca^{2+} extrusion pathway is electrogenic Ca^{2+} exchange that is either Na^+ dependent or Na^+ independent (likely H^+/Ca^{2+} exchange). In cardiac muscle, the Na^+-dependent Ca^{2+} extrusion (NCE; $3Na^+/Ca^{2+}$) dominates, with the highest maximum velocity (V_{max}) among tissues (Bernardi, 1999). There is a broad consensus that mitochondrial NCE is mediated by the $Na^+(Li^+)/Ca^{2+}$ exchanger (NCLX) (Boyman et al., 2013; Palty et al., 2010), while an electrogenic H^+/Ca^{2+} exchanger has yet to be found (LETM1 has been proposed as an electroneutral $2H^+/Ca^{2+}$ exchanger [Jiang et al., 2009; Tsai et al., 2014]). To avoid Ca^{2+} overload, effective MCUC activation is attained by higher $[Ca^{2+}]$ than the global $[Ca^{2+}]_c$ peaks in high $[Ca^{2+}]$ nanodomains at close contacts with the sarcoplasmic/endoplasmic reticulum (SR/ER), where Ca^{2+} release channels inositol 1,4,5-trisphosphate receptors and ryanodine receptors (RyR2s) locate (Rizzuto and Pozzan, 2006). In adult cardiac myocytes, these nanodomains locate at mitochondrial contacts with the SR terminal cisternae (junctional SR [jSR]) that form dyad junctions with sarcolemmal T tubules, where RyR2s face the L-type Ca^{2+} channels (Franzini-Armstrong, 2007). Mitochondrial matrix $[Ca^{2+}]$ ($[Ca^{2+}]_m$) signals activate matrix dehydrogenases that feed reducing equivalents to the electron transport chain and enhance ATP generation. This feed-forward loop to balance energy demands and supplies is referred to as cardiac excitation-energetics coupling (Balaban, 2002; Chacon et al., 1996; Csordás et al., 2001; Sharma et al., 2000).

We have recently reported that the MCUC is strategically positioned at the mitochondria-jSR contacts in adult cardiac muscle (De La Fuente et al., 2016). Because MCUC density is very low in cardiac mitochondria (Fieni et al., 2012), while the Na^+/Ca^{2+} exchanger is highly abundant, we hypothesized that co-localization of these transporters would lead to ineffective Ca^{2+} cycling, which is unfavorable for Ca^{2+} signaling. Here, we used multiple approaches to determine the spatial characteristics of NCLX distribution and NCE in the cardiac muscle mitochondria. We also pursued the idea that the separation of NCLX from MCUC hotspots would enhance the energy efficiency (i.e., lower the $\Delta\Psi_m$ expense) of generating $[Ca^{2+}]_m$ signals.

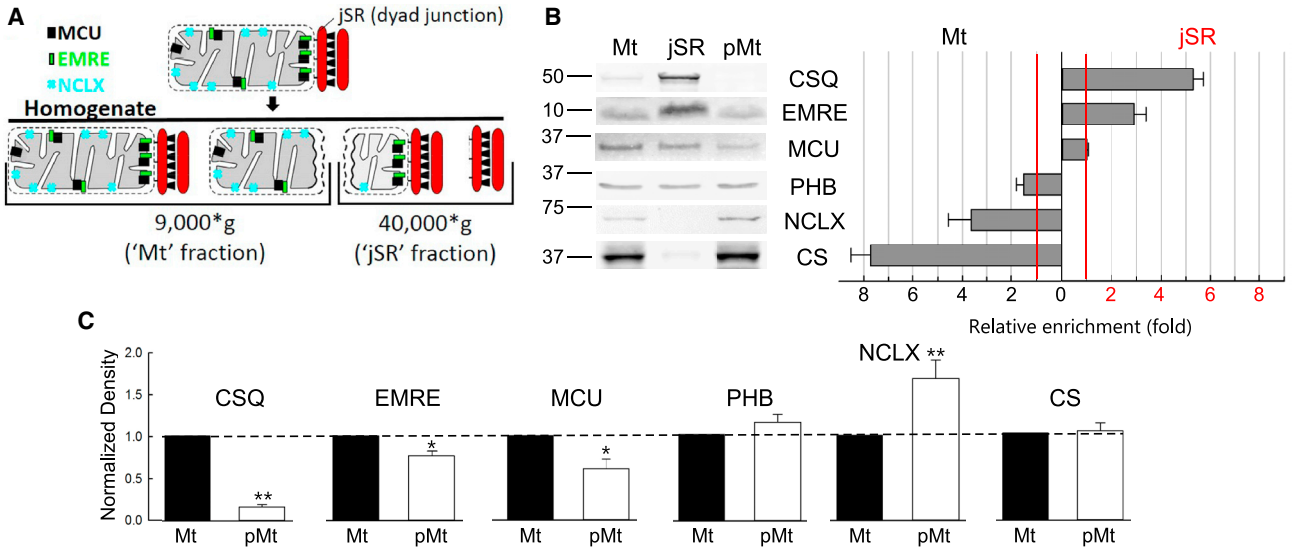

Figure 1. NCLX Levels Are Very Low in the jSR-Associated Mitochondrial Segments

(A) Schematics illustrating how mechanical homogenization of ventricular muscle yields mitochondria and mitochondrial fragments with different extents of jSR association in the mitochondrial (Mt) and jSR fractions (De La Fuente et al., 2016).

(B) Western blot analysis of the abundance of the indicated proteins in the rat heart crude Mt, jSR, and Percoll-purified Mt (pMt) fractions. Representative membrane images are on the left. The graph shows the cumulated band density (fold) differences between the Mt and jSR fractions. Bars representing proteins more abundant in the Mt or jSR fractions, respectively, point leftward and rightward. The red gridlines indicate the value of 1 (equal abundance). Means ± SEs, n = 4 rats.

(C) Quantitation of the Percoll purification of the mitochondrial fraction. Mean band densities after purification (pMt) are normalized to the levels before purification (Mt). Means ± SEs, n = 4 rats. *$p < 0.05$, **$p < 0.001$.

See also Figure S1.

RESULTS

NCLX Levels Are Low in the jSR-Associated Mitochondrial Segments

We established a fractionation-based model system to compare the proteins and Ca^{2+} transport of largely jSR-associated mitochondrial segments with whole mitochondria/mitochondrial segments not associated with jSR in the membrane fractions of ventricular homogenates. We used the "heavy SR" (jSR) fraction as the one enriched in jSR-associated mitochondrial segments and compared it to the (crude) mitochondrial fraction (Figure 1A) or that purified on Percoll gradient to clear out SR-bound particles (De La Fuente et al., 2016). MCU and EMRE both displayed higher abundance in the jSR than in the mitochondrial fraction (Figure 1B), while prohibitin, another integral inner mitochondrial membrane (IMM) protein, did not display such enrichment in the jSR fraction, and the matrix protein citrate synthase was severalfold more abundant in the mitochondrial fraction. NCLX levels were ~4-fold higher in the mitochondrial fraction than in the jSR fraction of rat heart (Figure 1B) and ~7-fold (7.2 ± 1.6, n = 4) in mouse heart. Percoll purification of the mitochondrial fraction effectively decreased the jSR marker calsequestrin, but not the citrate synthase levels (Figures 1B and 1C). The Coomassie blue-stained protein bands in the SDS gel showed consistent patterns with the purification; bands that weakened or disappeared in the purified mitochondria were strong in the jSR (Figure S1A, red marks), while those stronger in the purified mitochondria were weak or absent in the jSR fraction (Figure S1A, cyan marks). Percoll purification had opposing effects on the enrichment of MCUC components and NCLX; MCU and EMRE levels decreased in line with their preference for jSR-associated areas, whereas NCLX levels increased by the purification (Figures 1B and 1C). These data suggest a reciprocity between the distributions of the MCUC and the NCLX in the IMM. The MCUC preferentially locates at, while the NCLX seems to be excluded from the mitochondria-jSR contacts. Because membrane purification may adversely affect protein function, mitochondrial Ca^{2+} uptake and NCE were compared between crude and Percoll-purified mitochondrial fractions via fluorometric mitochondrial Ca^{2+} clearance assays. Crude and purified mitochondria both avidly sequestered Ca^{2+} when $[Ca^{2+}]$ in the medium ($[Ca^{2+}]_o$) was raised from ~0 to ~12 μM (Figure S1B). The initial rate of uptake ($[Ca^{2+}]_o$ decrease) was significantly higher in the crude mitochondria (270 ± 20 versus 190 ± 3 nM/s in the absence of Na^+), consistently with a decrease in MCUC components after purification. To probe NCE, when $[Ca^{2+}]_o$ reached near steady state, mitochondrial Ca^{2+} uptake was stopped by Ru360. This caused a steady increase in $[Ca^{2+}]_o$ in the presence but not or negligibly in the absence of Na^+ (10 mM), which was significantly faster in the Percoll-purified mitochondria, consistently with the higher NCLX abundance (Figures S1B, inset, and S1C).

Mitochondrial Ca^{2+} Uptake Is Strongly Countered by NCE in the Mitochondrial Fraction but Not in the jSR Fraction

Next, we tested whether the difference in NCLX protein levels between the fractions was translated to a corresponding difference in the mitochondrial NCE. To this end, two different sets

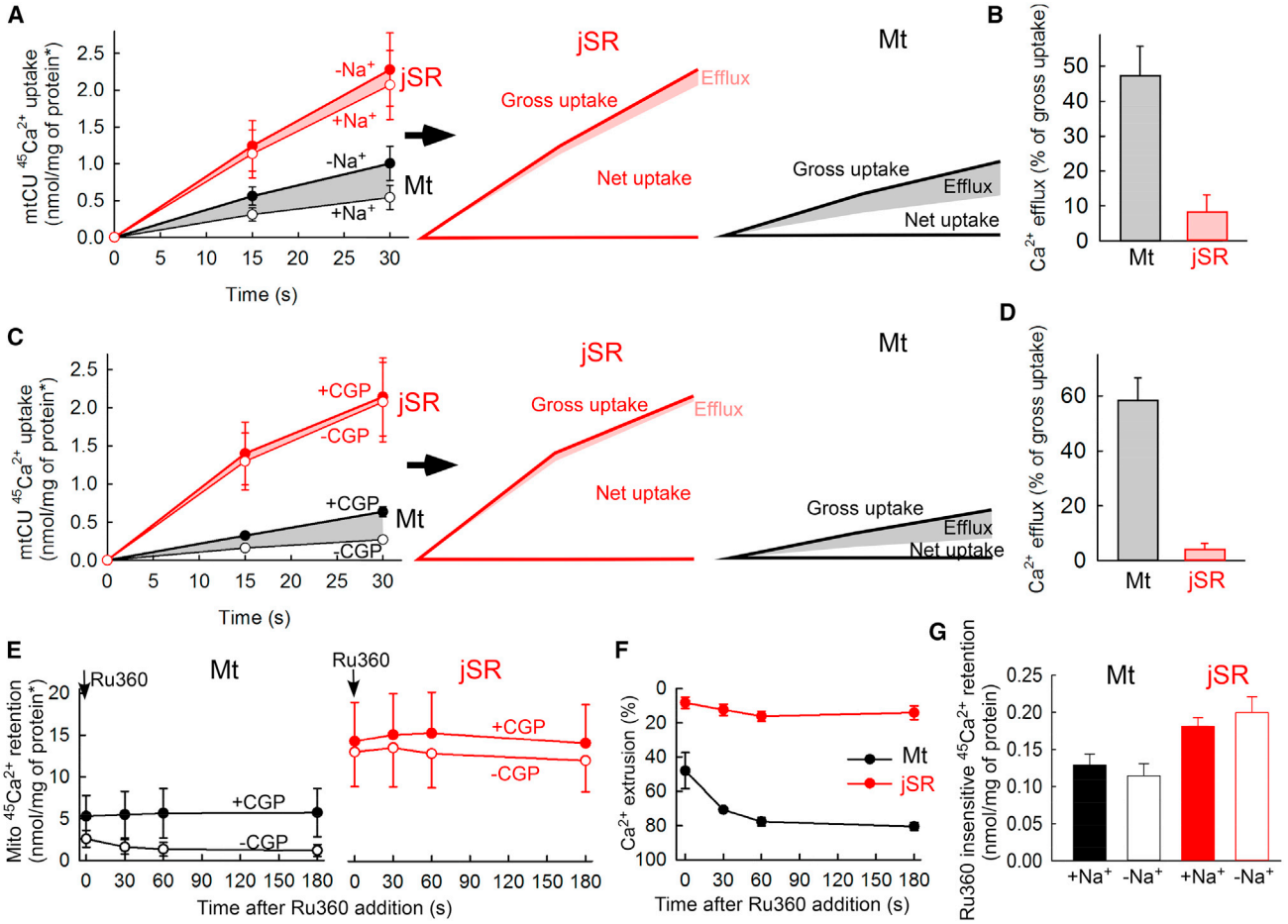

Figure 2. NCE Is Robust in the Mitochondrial Fraction, but Not in the jSR Fraction

(A–D) $^{45}Ca^{2+}$ retention assays assessing mitochondrial NCE based on how it counters MCUC-dependent Ca^{2+} uptake or (E and F) directly, based on the fractional loss in the sequestered $^{45}Ca^{2+}$ after suspending the uptake pharmacologically. To isolate mitochondrial Ca^{2+} fluxes, the SR was pre-depleted and the SERCA pumps blocked (pretreatment with thapsigargin 10 μM and caffeine 10 mM in the presence of 50 μM EGTA/Tris).

(A) MCUC-mediated (Ru360-sensitive) $^{45}Ca^{2+}$ uptake in the Mt (black) and jSR (red) fractions in the presence (+) and absence (–) of Na^+ (10 mM) at the indicated time points after increasing $[Ca^{2+}]$ in the assay buffer from virtually 0 to ~1.5 μM. The –Na^+ (no NCE) Ca^{2+} sequestration represents the "gross" unopposed Ca^{2+} uptake, while the +Na^+ (NCE active) Ca^{2+} sequestration is the "net" uptake, and the difference between the two is counted as the Na^+-dependent efflux (shaded areas in the graph). For clearer visualization of the proportions of gross and net uptake and the efflux in the jSR and Mt fractions, the corresponding graph segments are schematized on the right. Means ± SEs, n = 3–4 rats (triplicates). nmol/mg of protein*: to adjust to the difference in mitochondrial content between the fractions, a correction was applied based on the relative citrate synthase activity as outlined by De La Fuente et al. (2016).

(B) NCE from (A), expressed as the percentage of gross uptake.

(C and D) Gross and net MCUC-mediated $^{45}Ca^{2+}$ uptake and NCE determined and quantified as in (A) and (B), respectively, except that gross uptake is measured using the mitochondrial Na^+/Ca^{2+} exchanger inhibitor CGP-37157 (CGP 20 μM) in the presence of Na+.

(E) Following a 1-min period of $^{45}Ca^{2+}$ sequestration, as in (C), MCUC was blocked by adding Ru360 (10 μM), and the Ca^{2+} retained in the Mt and jSR fractions was measured at the indicated time points. To better isolate the Ca^{2+} loss due to mitochondrial NCE, the experiments were conducted both in the presence and absence of CGP.

(F) CGP-sensitive Ca^{2+} extrusion (difference between ± CGP) from (E), expressed as the percentage of (gross) Ca^{2+} retention at the time of Ru360 addition. Note that at time 0 there is already significant extrusion (as the gross minus net uptake difference). Means ± SEs, n = 3 rats (triplicates).

(G) MCUC-independent (Ru360-insensitive) Ca^{2+} retention in the Mt and jSR fractions determined from the 30-s points in (A) in the presence of Ru360.

See also Figure S2.

of mitochondrial $^{45}Ca^{2+}$ isotope retention assays were carried out using cardiac mitochondrial and jSR fractions. First, NCE was assessed indirectly from differential Ca^{2+}-uptake assays as the difference between gross (unopposed by NCE) and net (countered by NCE) uptakes. MCUC-mediated (Ru360-sensitive) $^{45}Ca^{2+}$ uptake from a Ca^{2+} bolus that raised $[Ca^{2+}]_o$ from ~0 to ~1.5 μM was determined and adjusted to the difference in active mitochondrial content of the membrane fractions (based on citrate synthase activity). To measure gross mitochondrial Ca^{2+} uptake, NCE was suspended either by omitting Na^+ (Figure 2A, solid symbols) or by the pharmacological inhibitor CGP-37157 (CGP; Figure 2C, solid symbols). Net uptake was

determined in the presence of Na^+ (10 mM), without CGP (Figures 2A and 2C, open symbols). The difference between gross and net uptakes (Figures 2A and 2C, shaded areas) was accounted for as the Na^+-dependent/CGP-sensitive Ca^{2+} efflux and normalized to the gross uptake (Figures 2B and 2D). Of note, the SR Ca^{2+} store was incapacitated pharmacologically (thapsigargin and caffeine), and the Ru360-insensitive $^{45}Ca^{2+}$ retention was very small and unaffected by the removal of Na^+ in both fractions (Figure 2G) (De La Fuente et al., 2016), indicating insignificant non-mitochondrial Ca^{2+} accumulation and NCE (e.g., contamination by sarcolemmal NCX1). The gross MCUC-mediated Ca^{2+} uptake was larger in the jSR fraction (Figures 2A and 2C), which is in line with MCUCs being clustered at the contacts with jSR (De La Fuente et al., 2016). NCE robustly countered the MCUC-mediated Ca^{2+} uptake in the mitochondrial fraction; ~50% of the gross uptake determined in the absence of Na^+ (Figures 2A and 2B) and ~60% of that determined under CGP inhibition (Figures 2A and 2B) was countered by NCE. By strong contrast, in the jSR fraction, only a small portion of the gross uptake (8.4% ± 4.8% in the absence of Na^+ [Figures 2A and 2B] and 4.2% ± 2.9% under CGP inhibition [Figures 2C and 2D]) was countered by NCE.

Second, to directly measure NCE from the mitochondria, we determined the CGP-sensitive decrease in $^{45}Ca^{2+}$ retention upon halting the uptake. After a 1-min uptake period, MCUC was blocked by Ru360, and a time course of the decrease in $^{45}Ca^{2+}$ retention was taken at 0, 30, 60, and 180 s (Figures 2E and 2F). NCE was then expressed as the residual $^{45}Ca^{2+}$ retention without CGP normalized to the corresponding retention under CGP inhibition. Consistent with the above-described $^{45}Ca^{2+}$ uptake assays, at the time of Ru360 addition (Figures 2E and 2F, 0 s in the time courses), the difference between gross and net MCUC-mediated uptake was <10% of the gross uptake in the jSR fraction and >50% in the mitochondrial fraction. In both fractions, the $^{45}Ca^{2+}$ efflux essentially reached steady state in 60 s, at 16% ± 3% and 78% ± 2.5% decrease in the sequestered Ca^{2+} in the jSR and mitochondrial fractions, respectively (Figure 2F). In both fractions, 80%–90% of the sequestered Ca^{2+} could be released by the combined addition of the uncoupler carbonyl-cyanide p-trifluoromethoxyphenylhydrazone (FCCP) and the Ca^{2+} ionophore ionomycin (not shown), indicating that the Ca^{2+} accumulated in the mitochondria remained releasable, and that most of the jSR-associated mitochondrial fragments in the jSR fraction were devoid of NCLX. The high retention of mitochondrial Ca^{2+} sequestered via MCUC and low CGP-sensitive Ca^{2+} efflux in the jSR fraction are again consistent with the NCLXs being excluded from the jSR-associated mitochondrial area where MCUC hotspots locate.

NCLX Ablation Diminishes NCE in the Mitochondrial Fraction

The data above show that the mitochondrial NCE is overwhelmingly more robust in the mitochondrial fraction than in the jSR fraction, which fits well with the multifold difference in NCLX; however, they are not direct evidence for causative connection. To validate that the NCE activity in the mitochondrial fraction is attributed to NCLX, we isolated the mitochondrial fraction from NCLX (*Slc8b1*)-depleted adult mouse hearts, using *Slc8b1*$^{fl/fl}$ × αMHC-MerCreMer (MCM) mice, in which NCLX is deleted selectively in cardiomyocytes after tamoxifen delivery (NCLX cKO), and from MCM control mouse hearts (Luongo et al., 2017). Then, we measured NCE as the difference between gross and net MCUC-mediated $^{45}Ca^{2+}$ uptake (Figures S2A and S2B). Compared to controls, the portion of gross MCUC-mediated Ca^{2+} uptake countered by NCE decreased by ~70% in the NCLX cKO (Figure S2C), which is consistent with earlier data in the same mouse model, showing ~70% decrease in NCLX expression after 10 days of tamoxifen administration (Luongo et al., 2017) (Figure S2D). These data confirm that NCLX is required for the robust NCE in cardiomyocyte mitochondria.

NCLX Overexpression Increases NCE in the Mitochondrial Fraction but Not in the jSR Fraction

Complementing the NCLX gene depletion studies and to further confirm that the robust NCE in the mitochondrial fraction was mediated by NCLX, we examined the impact of transgenic overexpression of NCLX. This approach also allowed us to assess whether overexpression could override the exclusion of NCLX from the jSR-associated mitochondrial areas. Cardiac mitochondrial and jSR fractions were isolated from mutant mice expressing the *SLC8B1* transgene only in adult cardiomyocytes (αMHC-tTA × TRE-NCLX) (Luongo et al., 2017). For the $^{45}Ca^{2+}$ retention assays, the mice were either receiving a doxycycline diet (control) or taken off it for 2 weeks (NCLX-overexpression [OE]), which resulted in an ~2.7-fold increase in NCLX protein expression (range, 1.7- to 3.8-fold differences between two control and two NCLX-OE animals) (Figure S2D). Mice overexpressing NCLX from the neonatal age (αMHC-tTA × TRE-NCLX kept on a normal diet) also overexpressed NCLX in this range (compared to the αMHC-tTA control) without compensatory increases in MCU or EMRE (Figure S3H). NCE (difference in gross and net MCUC-mediated uptake) in the mitochondrial fraction of the NCLX-OE mice displayed a substantial ~1.7-fold increase (39% ± 2% versus 23% ± 4%; Figure 3, black bars), further confirming the causative connection between the NCLX expression and NCE activity. By contrast, NCLX OE failed to increase NCE in the jSR fraction (remained not significantly different from zero; Figures 3B and 3C, red bars), suggesting that NCLX is effectively expelled from the jSR-associated mitochondrial segments by a mechanism that is not limited by the NCLX quantity within the tested range. Accordingly, NCLX protein levels remained very low in the jSR fraction of NCLX OE mice (Figures S2E and S3H). The gross mitochondrial morphology and morphometry of the mitochondrial contacts with the jSR were not noticeably affected by the NCLX OE based on transmission electron micrographic evaluation of longitudinal sections of the left ventricular wall (Figures S3A–S3G).

The Energy Efficiency of $[Ca^{2+}]_m$ Signal Generation in Cells with Non-polarized Submitochondrial MCUC Distribution Decreases upon NCLX OE

With this reciprocity between MCUC and NCLX in localization preference toward the mitochondria-jSR interface area in the cardiac mitochondria, we sought evidence for the biological significance of such a peculiar distribution. We approached this from the perspective of $[Ca^{2+}]_m$ signal generation efficacy and energy cost. The electrogenic MCUC and NCLX use the driving

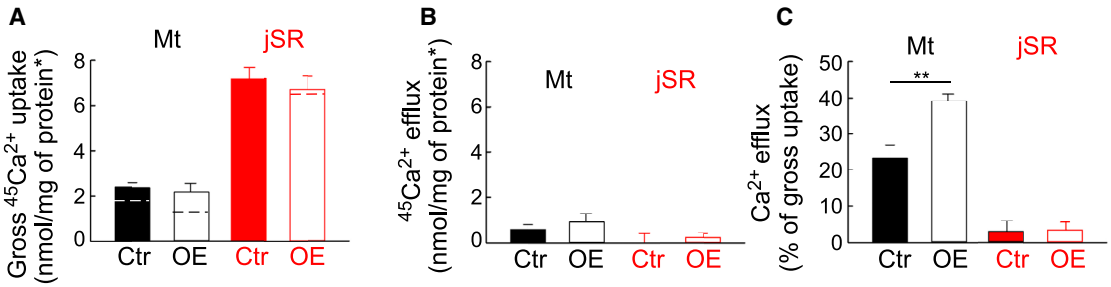

Figure 3. Transgenic Overexpression of NCLX Increases NCE in the Mitochondrial Fraction, but Not in the jSR Fraction

NCE in the cardiac mitochondrial and jSR fraction of control (Ctr) mice and those with adult cardiomyocyte-specific NCLX overexpression (OE) was determined by means of identical $^{45}Ca^{2+}$ retention assays, as in Figures 2A and 2B.

(A) Gross ($-Na^+$) mitochondrial Ca^{2+} uptakes at 30 s. Net ($+Na^+$) uptake levels are indicated with dashed lines.

(B) Na^+-dependent efflux (NCE) as the difference between gross and net uptakes.

(C) Na^+-dependent efflux as the percentage of the gross uptake. Note the significant increase in the fractional efflux in the mitochondrial (black) but not in the jSR (red) fraction. Bar charts are means ± SEs, n = 3 Ctr and 3 OE mice (triplicates for each).

*$p < 0.05$, **$p < 0.001$. See also Figures S2, S3, and S5F.

force (energy) of $\Delta\Psi_m$ to mediate opposing Ca^{2+} fluxes that largely determine $[Ca^{2+}]_m$. While the MCUC gating is tightly regulated and the activation is limited by a $[Ca^{2+}]_c$ threshold, NCLX is readied constitutively and will work against basically any $[Ca^{2+}]_m$ rise in a Na^+-dependent manner (De Stefani et al., 2016). We postulated, when NCLX is near the MCUC, from the start of $[Ca^{2+}]_m$ signal development $\Delta\Psi_m$ would be used concurrently for both Ca^{2+} uptake and extrusion, thus accelerating depolarization while slowing net uptake. Conversely, if MCUC is distanced from NCLX, then, upon a short local Ca^{2+} exposure from the dyad, $\Delta\Psi_m$ could be used sequentially for uptake and then extrusion, with slower depolarization but faster net uptake, making signaling more energy efficient.

Because experimental modeling of the separation of NCLX and MCU is very difficult, we decided to test whether OE of NCLX in a cell model with evenly distributed MCUC would increase the energy ($\Delta\Psi_m$) expense of generating a $[Ca^{2+}]_m$ signal in a given time frame. We thus studied the $\Delta\Psi_m$ and $[Ca^{2+}]_m$ responses to a $[Ca^{2+}]_c$ rise evoked by a $CaCl_2$ bolus via fluorescence imaging in a permeabilized cell system. Control and NCLX-FLAG-transfected (NCLX-OE) H9c2 cardiac myoblasts were compared. We chose the H9c2 cells because they have sufficiently robust mitochondrial Ca^{2+} uptake (MCUC) and CGP-sensitive Ca^{2+} extrusion (NCLX) systems (Pacher et al., 2000; Szalai et al., 2000). In contrast to the hotspots at the jSR-associated transversal side of interfibrillar mitochondria in the adult cardiomyocytes (De La Fuente et al., 2016), the immunofluorescence of MCU showed a diffuse distribution over the mitochondria in the H9c2 cells as resolved via confocal Airyscan imaging (Zeiss; Figure S4A). The overexpressed NCLX-FLAG displayed mitochondrial localization (Figure S4B).

Via multiparameter wide-field electron-multiplying charge-coupled device (EMCCD) imaging in gently permeabilized cells, $[Ca^{2+}]_c$ ($[Ca^{2+}]$ in the intracellular medium) was monitored using Fura-2 LoAff, $\Delta\Psi_m$ using tetramethylrhodamine methyl ester (TMRM), and $[Ca^{2+}]_m$ using either Rhod-2-acetyoxymethyl ester (rhod-2/AM) separately from TMRM (Figure 4) or together via transiently (co)transfected mitochondrial matrix-targeted genetically engineered Ca^{2+} indicator CEPIA3mt (Figures S5A–S5E). Upon increasing $[Ca^{2+}]_c$ to ~5 μM, $[Ca^{2+}]_m$ displayed a rapid upstroke followed by a gradual increase to the peak (Figure 4A). The time to peak (max$[Ca^{2+}]_m$) was significantly longer in the NCLX-OE cells, indicating stronger hindering of the MCUC-mediated net mitochondrial Ca^{2+} uptake by NCE. Also, in the absence of Na^+, the time to peak was significantly shorter and the difference between control and NCLX-OE cells disappeared (Figure 4B, $+Na^+$ versus $-Na^+$). During the slow rising phase and the post-peak plateau, at steadily high $[Ca^{2+}]_c$ (due to the quasi-infinite incubation volume compared to the volume of the cells), mitochondrial Ca^{2+} uptake overwhelmed NCE. When $[Ca^{2+}]_c$ was returned to the low nanomolar range (below the MCUC activation threshold) using the Ca^{2+} chelator EGTA, $[Ca^{2+}]_m$ began to decrease, and, as expected, this decrease was much faster in the NCLX-OE cells in the presence of Na^+ (Figures 4A and 4C). Without Na^+ there was a small residual Ca^{2+} extrusion that was not significantly different between Ctr and NCLX OE; thus, it was likely mediated by a mechanism other than NCE (e.g., the H^+/Ca^{2+} exchange). Despite slower $[Ca^{2+}]_m$ rise to peak, the associated IMM depolarization in the NCLX-OE cells was faster and larger in the recorded time frame (Figures 4D and 4E). After the EGTA addition that stopped the mitochondrial Ca^{2+} uptake, an IMM repolarization occurred, which in Ctr cells was close to complete in ~2 min (after correcting to a baseline drift), whereas in the NCLX-OE cells there was still substantial residual depolarization (Figures 4D and 4F). This difference in residual repolarization disappeared in the absence of Na^+, suggesting that it was caused by the high electrogenic NCLX activity. This also confirms that in the plateau phase of the $[Ca^{2+}]_m$ rise, mitochondrial Ca^{2+} uptake and NCE both were active. Significant activation of the permeability transition pore was not likely because in that case, the added EGTA would have rapidly chelated $[Ca^{2+}]_m$; however, rapid lowering of $[Ca^{2+}]_m$ by EGTA only occurred in the NCLX-OE cells in the presence but not absence of Na^+, which is indicative of NCE. Similar tendencies were observed when $[Ca^{2+}]_m$ and $\Delta\Psi_m$ were simultaneously recorded using CEPIA3mt and TMRM (Figures S5A–S5E), although in this case, the $[Ca^{2+}]_c$ stimulus that led to strong depolarization in both Ctr and NCLX-OE cells by the time of the EGTA addition

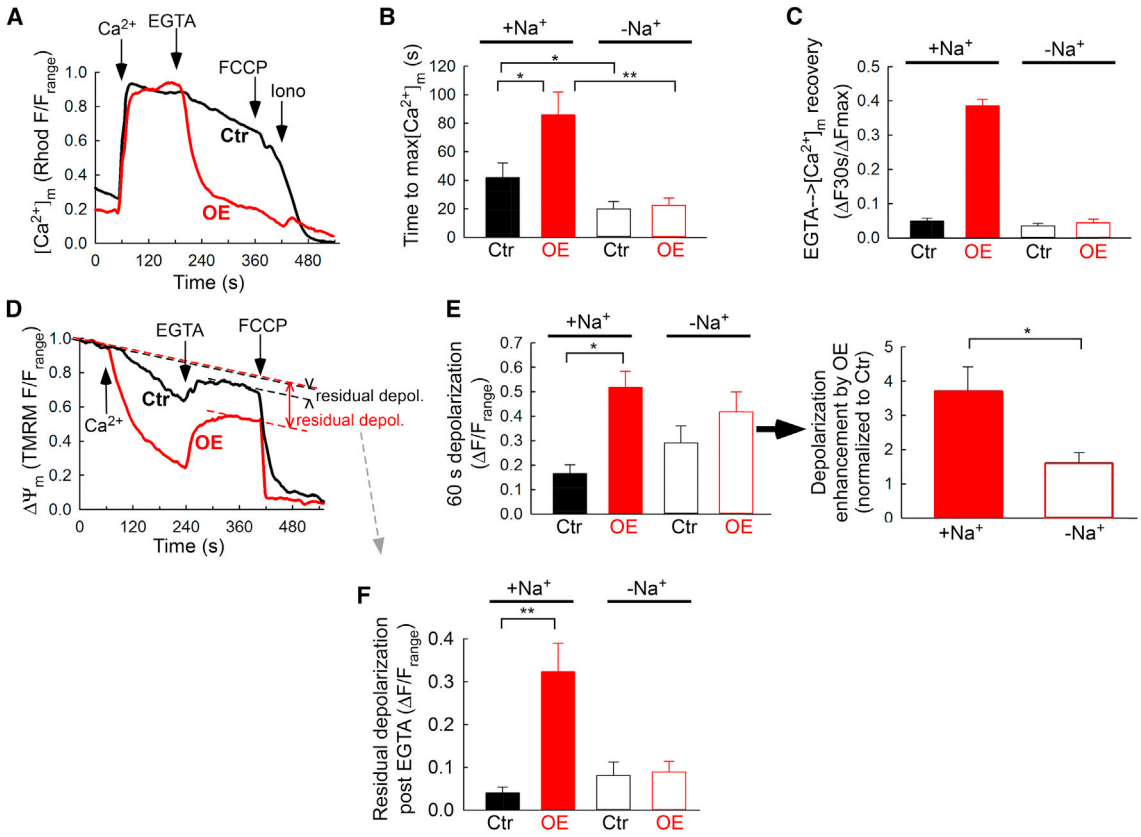

Figure 4. NCLX, When Not Separated from MCUC, Increases the Energy Cost of Mitochondrial Ca^{2+} Signal Generation

H9c2 myoblasts (with non-polarized MCU distribution; Figure S4), transiently transfected with NCLX-FLAG (NCLX-OE, OE) or control vector (Ctr), were loaded with rhod-2/AM or TMRM to record $[Ca^{2+}]_m$ and $\Delta\Psi_m$, respectively, then gently permeabilized. Fluorescence time courses were taken using a wide-field microscope fitted with an EMCCD camera. To isolate mitochondrial Ca^{2+} handling, the ER was pre-depleted with thapsigargin (2 μM). After 1-min baseline recording in virtually Ca^{2+}-free intracellular buffer (supplemented with 10 μM EGTA), $[Ca^{2+}]$ in the buffer ($[Ca^{2+}]_c$) was raised to ~5 μM (determined by Fura-LoAff, not shown) by a $CaCl_2$ bolus (20 μM) for a period of 2–2.5 min (2 min in A). In turn, $[Ca^{2+}]_c$ was chelated down to the low nanomolar range by adding 100 μM EGTA/Tris (pH 7.4) to suspend further mitochondrial Ca^{2+} uptake and facilitate extrusion. Three minutes later, the mitochondrial uncoupler FCCP and the Ca^{2+} ionophore ionomycin were added to dissipate $\Delta\Psi_m$ and release the Ca^{2+} from the matrix.

(A) Representative time courses of $[Ca^{2+}]_m$ (rhod-2 fluorescence normalized to the range F_{max}–F_{min}) recorded in control and NCLX-OE cells in Na^+-containing medium.

(B) Bar chart showing the time to peak $[Ca^{2+}]_m$ in the presence and absence of Na^+.

(C) Fractional recovery of the $[Ca^{2+}]_m$ rise 30 s after EGTA addition.

(D) Representative time courses of $\Delta\Psi_m$ (F_{TMRM} normalized to the range F_{max}–F_{min}) recorded in Ctr and NCLX-OE cells in Na^+-containing medium.

(E) Left bar chart shows the $\Delta\Psi_m$ loss (from D) 60 s after the $CaCl_2$ addition in the presence and absence of Na^+. The fold enhancement of the depolarization by the NCLX OE relative to Ctr is shown on the right.

(F) Residual depolarization after returning $[Ca^{2+}]_c$ to the low nanomolar range with EGTA in the experiments shown in (D). The values, as depicted in (D) by the red (OE) double-headed arrow and black opposing arrowheads (Ctr), are corrected to a baseline drift (shown in D by dashed linear fits to the initial period and to the post-EGTA quasi-steady-state period). Bar charts are means ± SEs, n = 3 independent experiments (1–3 technical replicates each).

(B, E, and F) *$p < 0.05$, **$p < 0.001$.

See also Figures S4 and S5.

was larger (~7 μM); this was followed by only moderate repolarization during the recording period. These experiments confirm that the energy ($\Delta\Psi_m$) cost of a $[Ca^{2+}]_m$ rise is higher when NCLX levels are increased in mitochondria with non-polarized MCUC distribution.

DISCUSSION

Here, we report reciprocal distribution patterns between the primary mitochondrial Ca^{2+} uptake and extrusion mechanisms, MCUC and NCLX, in the cardiac muscle. While MCUC is strategically concentrated to the area of mitochondria-jSR association to facilitate local Ca^{2+} delivery (De La Fuente et al., 2016), these areas are mostly devoid of the otherwise highly abundant NCLX. We find the NCLX protein severalfold more abundant in the mitochondrial fraction containing mitochondria with little or no jSR contact than in the jSR fraction containing mitochondria with extensive jSR contacts. Further purification that clears SR-connected segments from the mitochondrial fraction increases the NCLX enrichment but decreases the levels of MCU and EMRE.

In line with the differential protein distribution, $^{45}Ca^{2+}$ flux assays confirmed that the mitochondrial NCE is largely diminished in the mitochondria of the jSR fraction. NCE in the mitochondrial fraction was diminished by NCLX ablation and strengthened by transgenic NCLX OE, supporting the notion that the cardiac mitochondrial NCE is mostly mediated by NCLX (Boyman et al., 2013; Luongo et al., 2017).

We propose that the separation of mitochondrial Ca^{2+} uptake hotspots from the Ca^{2+} extrusion sites in cardiomyocytes is highly relevant as a cooperative measure to enhance the efficiency of $[Ca^{2+}]_m$ signal generation and excitation-energetics coupling. MCUC (current) density in the cardiac IMM is one of the smallest among many tissues (Fieni et al., 2012), while the cardiac mitochondrial NCE is one of the most robust (Bernardi, 1999). As schematized in Figure S5F, excluding NCLX from the exposure area of local jSR-derived $[Ca^{2+}]_c$ signaling where MCUC is concentrated permits a larger portion of Ca^{2+} entering the matrix to effectively raise a $[Ca^{2+}]_m$ signal. NCLX included in this location would remove locally a fraction of the Ca^{2+} entering through the MCUC. This fraction would not contribute to the bulk $[Ca^{2+}]_m$ signal, leading to smaller $[Ca^{2+}]_m$ response to the same local $[Ca^{2+}]_c$ signal, despite consuming the same $\Delta\Psi_m$ (the situation depicted in Figure S5F, bottom). This would compromise the efficiency of excitation-energetics coupling. This principle was demonstrated using the NCLX-OE H9c2 cells, in which a given $[Ca^{2+}]_m$ rise (signal) required more Ca^{2+} to cycle through the matrix, hence higher consumption of $\Delta\Psi_m$ (depolarization) and a higher energy cost of signal generation (Figures 4 and S5A–S5E). In line with the energy-efficient arrangement between MCUC and NCLX activities in the heart, an earlier study of patch-clamped cardiomyocytes found no loss in $\Delta\Psi_m$ upon enhancement of NCE activity (by increasing $[Na^+]_c$) when electrically paced under basal and β-adrenergic-stimulated conditions (Maack et al., 2006).

The significance of cardiac mitochondrial Ca^{2+} signaling has been challenged by the lack of major cardiac phenotype upon germline ablation of MCU (Holmström et al., 2015; Pan et al., 2013), but the constitutive loss of MCUC function may prompt significant adaptation (Rasmussen et al., 2015). Short-term genetic loss-of-function studies in adult mice revealed a significant role for MCUC-mediated mitochondrial Ca^{2+} uptake in the bioenergetic adaptation to stress (Kwong et al., 2015; Luongo et al., 2015; Wu et al., 2015). The importance of baseline cardiac mitochondrial Ca^{2+} cycling via MCUC and NCLX is underscored by recent reports that raising the MCUC $[Ca^{2+}]_c$ activation threshold via MICU1 OE impaired contractile function (Paillard et al., 2017), while NCLX ablation in the adult mouse heart led to lethal cardiomyopathy (Luongo et al., 2017). Likely due to its topology (RyR2 faces the dyadic and not the jSR-mitochondrial cleft), only a small fraction of the RyR2-mediated Ca^{2+} release is sequestered via the MCUC (Boyman et al., 2014). Thus, effective $[Ca^{2+}]_m$ signaling is critical for excitation-energetics coupling, for which MCUC and NCLX must be optimally coordinated spatially and temporally.

To identify the mechanism(s) keeping NCLX out of the contact areas with jSR, further studies on its molecular interactions will be needed. One important clue is that transgenic OE could not significantly mitigate the expulsion of NCLX, indicating a robust, high-capacity mechanism (e.g., local degradation, active targeting to non-jSR-associated areas).

While visualizing NCLX distribution *in situ* would complement our fractionation-based data well, to date we are not aware of any anti-NCLX antibody that is suitable to detect the native murine NCLX *in situ* (by immunofluorescence). Our screening of the current commercial NCLX antibody lineup is summarized in Table S1, which confirms some new antibodies for western blot, but none without serious cross-reactions preventing the *in situ* visualization (immunofluorescence, not shown).

Redistribution of mitochondrial proteins to facilitate local communication is a broader phenomenon of mitochondrial integration with the local cellular environment. Mitochondria engage in local contacts with multiple diverse partners (Csordás et al., 2018). Proteins responsible for recruiting nucleoids to ER contact sites (Lewis et al., 2016) and intermitochondrial contact proteins that enable cardiac mitochondria to form an electrical grid (Glancy et al., 2017) and/or mediate transmitochondrial cristae alignment (Picard et al., 2015) are likely locally concentrated. Besides enhancing the efficacy of $[Ca^{2+}]_m$ signal generation, the peculiar distribution differences between mitochondrial Ca^{2+} uptake and extrusion sites in the adult cardiac muscle seem to mirror distribution differences in the SR Ca^{2+} release (RyR2) and uptake (sarco-endoplasmic reticulum Ca^{2+} ATPase [SERCA]) concentrated to the jSR and network SR, respectively (Greenstein and Winslow, 2011). In some cell types, mitochondrial NCE has been proposed to feed Ca^{2+} to SERCA pumps (Malli et al., 2005; Poburko et al., 2009). It is for future studies to clarify whether distinct communication with the mitochondrion-associated jSR and network SR could control the distribution of MCUC and NCLX.

STAR★METHODS

Detailed methods are provided in the online version of this paper and include the following:

- KEY RESOURCES TABLE
- CONTACT FOR REAGENT AND RESOURCES SHARING
- EXPERIMENTAL MODEL AND SUBJECT DETAILS
  - Mice and rats
  - Cell culture and DNA transfection
- METHOD DETAILS
  - Heart Mitochondria and jSR Isolation
  - $45Ca^{2+}$ Retention Assays
  - Fluorescence wide field imaging
  - Protein Analysis and western blot
  - Fluorometric Measurements of $[Ca^{2+}]_o$
  - Immunofluorescence of H9C2 Cells
  - TEM
- QUANTIFICATION AND STATISTICAL ANALYSIS

SUPPLEMENTAL INFORMATION

Supplemental Information includes five figures and one table and can be found with this article online at https://doi.org/10.1016/j.celrep.2018.08.040.

ACKNOWLEDGMENTS

We thank Timothy Luongo and Trevor Tierney for helping with the sample isolation and preparation of the NCLX cKO and NCLX-OE animals. We thank David Weaver, director of technology development at the MitoCare Center, for helping with the custom ImageJ plug-in for the transmission electron microscopic (TEM) morphometric analysis of mitochondria-jSR contacts and critical reading of the manuscript. We also thank Gyorgy Hajnoczky and Erin L. Seifert for helpful discussions and critical reading of the manuscript. This work was funded by the NIH, National Heart, Lung, and Blood Institute (NHLBI) (R01HL122124, to G.C.; R01HL123966, R01HL136954, R01HL142271, and P01HL134608 sub-5483, to J.W.E.; R01HL093671, R01HL122124, and R01HL137266, to S.-S.S.), and by the American Heart Association (16POST27770032, to S.D.L.F.; 17PRE33460423 to J.P.L.).

AUTHOR CONTRIBUTIONS

S.D.L.F. designed and performed the experiments, analyzed and interpreted the data, created the figures, and wrote the manuscript. J.P.L. provided the NCLX cKO and NCLX-OE mice, isolated the cardiomyocytes, helped S.D.L.F. with tissue isolation and fractionation at Temple University and with the NCLX antibody tests, and read the manuscript. Z.N. performed the FLAG immunofluorescence experiments and all steps of the electron microscopy, and wrote the manuscript. C.F.S. performed citrate synthase activity assays and read the manuscript. J.W.E. supervised the experiments at Temple University, interpreted the data, and read and edited the manuscript. S.-S.S. designed and supervised the experiments, interpreted the data, and read and edited the manuscript. G.C. conceived the work, designed and supervised the experiments, interpreted the data, and wrote the manuscript.

DECLARATION OF INTERESTS

The authors declare no competing interests.

Received: December 15, 2017
Revised: June 28, 2018
Accepted: August 15, 2018
Published: September 18, 2018

REFERENCES

Balaban, R.S. (2002). Cardiac energy metabolism homeostasis: role of cytosolic calcium. J. Mol. Cell. Cardiol. *34*, 1259–1271.

Bernardi, P. (1999). Mitochondrial transport of cations: channels, exchangers, and permeability transition. Physiol. Rev. *79*, 1127–1155.

Boyman, L., Williams, G.S., Khananshvili, D., Sekler, I., and Lederer, W.J. (2013). NCLX: the mitochondrial sodium calcium exchanger. J. Mol. Cell. Cardiol. *59*, 205–213.

Boyman, L., Chikando, A.C., Williams, G.S., Khairallah, R.J., Kettlewell, S., Ward, C.W., Smith, G.L., Kao, J.P., and Lederer, W.J. (2014). Calcium movement in cardiac mitochondria. Biophys. J. *107*, 1289–1301.

Cai, X., and Lytton, J. (2004). Molecular cloning of a sixth member of the K+-dependent Na+/Ca2+ exchanger gene family, NCKX6. J. Biol. Chem. *279*, 5867–5876.

Chacon, E., Ohata, H., Harper, I.S., Trollinger, D.R., Herman, B., and Lemasters, J.J. (1996). Mitochondrial free calcium transients during excitation-contraction coupling in rabbit cardiac myocytes. FEBS Lett. *382*, 31–36.

Csordás, G., Thomas, A.P., and Hajnóczky, G. (2001). Calcium signal transmission between ryanodine receptors and mitochondria in cardiac muscle. Trends Cardiovasc. Med. *11*, 269–275.

Csordás, G., Weaver, D., and Hajnóczky, G. (2018). Endoplasmic reticulum-mitochondrial contactology: structure and signaling functions. Trends Cell Biol. *28*, 523–540.

De La Fuente, S., Fernandez-Sanz, C., Vail, C., Agra, E.J., Holmstrom, K., Sun, J., Mishra, J., Williams, D., Finkel, T., Murphy, E., et al. (2016). Strategic positioning and biased activity of the mitochondrial calcium uniporter in cardiac muscle. J. Biol. Chem. *291*, 23343–23362.

De Stefani, D., Rizzuto, R., and Pozzan, T. (2016). Enjoy the trip: calcium in mitochondria back and forth. Annu. Rev. Biochem. *85*, 161–192.

Fieni, F., Lee, S.B., Jan, Y.N., and Kirichok, Y. (2012). Activity of the mitochondrial calcium uniporter varies greatly between tissues. Nat. Commun. *3*, 1317.

Franzini-Armstrong, C. (2007). ER-mitochondria communication. How privileged? Physiology (Bethesda) *22*, 261–268.

Glancy, B., Hartnell, L.M., Combs, C.A., Femnou, A., Sun, J., Murphy, E., Subramaniam, S., and Balaban, R.S. (2017). Power grid protection of the muscle mitochondrial reticulum. Cell Rep. *19*, 487–496.

Greenstein, J.L., and Winslow, R.L. (2011). Integrative systems models of cardiac excitation-contraction coupling. Circ. Res. *108*, 70–84.

Holmström, K.M., Pan, X., Liu, J.C., Menazza, S., Liu, J., Nguyen, T.T., Pan, H., Parks, R.J., Anderson, S., Noguchi, A., et al. (2015). Assessment of cardiac function in mice lacking the mitochondrial calcium uniporter. J. Mol. Cell. Cardiol. *85*, 178–182.

Jiang, D., Zhao, L., and Clapham, D.E. (2009). Genome-wide RNAi screen identifies Letm1 as a mitochondrial Ca2+/H+ antiporter. Science *326*, 144–147.

Kamer, K.J., and Mootha, V.K. (2015). The molecular era of the mitochondrial calcium uniporter. Nat. Rev. Mol. Cell Biol. *16*, 545–553.

Kwong, J.Q., Lu, X., Correll, R.N., Schwanekamp, J.A., Vagnozzi, R.J., Sargent, M.A., York, A.J., Zhang, J., Bers, D.M., and Molkentin, J.D. (2015). The mitochondrial calcium uniporter selectively matches metabolic output to acute contractile stress in the heart. Cell Rep. *12*, 15–22.

Lewis, S.C., Uchiyama, L.F., and Nunnari, J. (2016). ER-mitochondria contacts couple mtDNA synthesis with mitochondrial division in human cells. Science *353*, aaf5549.

Luongo, T.S., Lambert, J.P., Yuan, A., Zhang, X., Gross, P., Song, J., Shanmughapriya, S., Gao, E., Jain, M., Houser, S.R., et al. (2015). The mitochondrial calcium uniporter matches energetic supply with cardiac workload during stress and modulates permeability transition. Cell Rep. *12*, 23–34.

Luongo, T.S., Lambert, J.P., Gross, P., Nwokedi, M., Lombardi, A.A., Shanmughapriya, S., Carpenter, A.C., Kolmetzky, D., Gao, E., van Berlo, J.H., et al. (2017). The mitochondrial Na^+/Ca^{2+} exchanger is essential for Ca^{2+} homeostasis and viability. Nature *545*, 93–97.

Maack, C., Cortassa, S., Aon, M.A., Ganesan, A.N., Liu, T., and O'Rourke, B. (2006). Elevated cytosolic Na+ decreases mitochondrial Ca2+ uptake during excitation-contraction coupling and impairs energetic adaptation in cardiac myocytes. Circ. Res. *99*, 172–182.

Malli, R., Frieden, M., Trenker, M., and Graier, W.F. (2005). The role of mitochondria for Ca2+ refilling of the endoplasmic reticulum. J. Biol. Chem. *280*, 12114–12122.

Mammucari, C., Gherardi, G., and Rizzuto, R. (2017). Structure, activity regulation, and role of the mitochondrial calcium uniporter in health and disease. Front. Oncol. *7*, 139.

Mishra, J., Jhun, B.S., Hurst, S., O-Uchi, J., Csordás, G., and Sheu, S.-S. (2017). The mitochondrial Ca2+ uniporter: structure, function, and pharmacology. Handb. Exp. Pharmacol. *240*, 129–156.

Pacher, P., Csordás, P., Schneider, T., and Hajnóczky, G. (2000). Quantification of calcium signal transmission from sarco-endoplasmic reticulum to the mitochondria. J. Physiol. *529*, 553–564.

Paillard, M., Csordás, G., Szanda, G., Golenár, T., Debattisti, V., Bartok, A., Wang, N., Moffat, C., Seifert, E.L., Spät, A., and Hajnóczky, G. (2017). Tissue-specific mitochondrial decoding of cytoplasmic Ca^{2+} signals is controlled by the stoichiometry of MICU1/2 and MCU. Cell Rep. *18*, 2291–2300.

Palty, R., Silverman, W.F., Hershfinkel, M., Caporale, T., Sensi, S.L., Parnis, J., Nolte, C., Fishman, D., Shoshan-Barmatz, V., Herrmann, S., et al. (2010). NCLX is an essential component of mitochondrial Na+/Ca2+ exchange. Proc. Natl. Acad. Sci. USA *107*, 436–441.

Pan, X., Liu, J., Nguyen, T., Liu, C., Sun, J., Teng, Y., Fergusson, M.M., Rovira, I.I., Allen, M., Springer, D.A., et al. (2013). The physiological role of mitochondrial calcium revealed by mice lacking the mitochondrial calcium uniporter. Nat. Cell Biol. *15*, 1464–1472.

Picard, M., McManus, M.J., Csordás, G., Várnai, P., Dorn, G.W., 2nd, Williams, D., Hajnóczky, G., and Wallace, D.C. (2015). Trans-mitochondrial coordination of cristae at regulated membrane junctions. Nat. Commun. *6*, 6259.

Poburko, D., Liao, C.H., van Breemen, C., and Demaurex, N. (2009). Mitochondrial regulation of sarcoplasmic reticulum Ca2+ content in vascular smooth muscle cells. Circ. Res. *104*, 104–112.

Rasmussen, T.P., Wu, Y., Joiner, M.L., Koval, O.M., Wilson, N.R., Luczak, E.D., Wang, Q., Chen, B., Gao, Z., Zhu, Z., et al. (2015). Inhibition of MCU forces extramitochondrial adaptations governing physiological and pathological stress responses in heart. Proc. Natl. Acad. Sci. USA *112*, 9129–9134.

Rizzuto, R., and Pozzan, T. (2006). Microdomains of intracellular Ca2+: molecular determinants and functional consequences. Physiol. Rev. *86*, 369–408.

Sharma, V.K., Ramesh, V., Franzini-Armstrong, C., and Sheu, S.S. (2000). Transport of Ca2+ from sarcoplasmic reticulum to mitochondria in rat ventricular myocytes. J. Bioenerg. Biomembr. *32*, 97–104.

Suzuki, J., Kanemaru, K., Ishii, K., Ohkura, M., Okubo, Y., and Iino, M. (2014). Imaging intraorganellar Ca2+ at subcellular resolution using CEPIA. Nat. Commun. *5*, 4153.

Szalai, G., Csordás, G., Hantash, B.M., Thomas, A.P., and Hajnóczky, G. (2000). Calcium signal transmission between ryanodine receptors and mitochondria. J. Biol. Chem. *275*, 15305–15313.

Tsai, M.F., Jiang, D., Zhao, L., Clapham, D., and Miller, C. (2014). Functional reconstitution of the mitochondrial Ca2+/H+ antiporter Letm1. J. Gen. Physiol. *143*, 67–73.

Wu, Y., Rasmussen, T.P., Koval, O.M., Joiner, M.L., Hall, D.D., Chen, B., Luczak, E.D., Wang, Q., Rokita, A.G., Wehrens, X.H., et al. (2015). The mitochondrial uniporter controls fight or flight heart rate increases. Nat. Commun. *6*, 6081.

STAR★METHODS

KEY RESOURCES TABLE

REAGENT or RESOURCE	SOURCE	IDENTIFIER
Antibodies		
Alexa fluor 488 chicken anti rabbit	Invitrogene	Cat. #A21441; RRID: AB_2535859
Alexa fluor 647 donkey anti mouse	Invitrogene	Cat. #A31571; RRID: AB_162542
Anti-calsequestrin	Abcam	Cat. #ab3516; RRID: AB_303865
Anti-EMRE	Santa cruz	Cat. #sc86337; RRID: AB_2250685
Anti-flag	Sigma-aldrich	Cat. #F1804-1MG; RRID: AB_262044
Anti-MCU	Cell signaling	Cat. #CSTD2Z3B; RRID: AB_2721812
Anti-NCLX antibodies	See Table S1	N/A
Anti-prohibitin	Abcam	Cat. #ab28172; RRID: AB_777457
IRDye 800CW	Li-Cor	Cat. #926-32213; RRID: AB_621848
Biological Samples		
Cardiac mitochondria and jSR isolated from mouse and rat heart	(De La Fuente et al., 2016)	N/A
Chemicals, Peptides, and Recombinant Proteins		
Adenosine 5′-triphosphate magnesium salt	Sigma-Aldrich	Cat. #A9187
Ammonium Persulfate (APS)	Thermo Fisher Scientific	Cat. # 17874
Antipain dihydrochloride from microbial source	Sigma-Aldrich	Cat. #A6191-5mg
Bovine Serum Albumine	Sigma-Aldrich	Cat. #03116964001
Calcium-45 Radionuclide, Calcium Chloride in Aqueous Solution	Perkin-Elmer	Cat. #NEZ013001MC
Calcium chloride solution	Sigma-Aldrich	Cat. #21115
Caffeine	Sigma-Aldrich	Cat. #C0750-500 g
CGP 37157	Enzo Life Sciences	Cat. #BML-CM119-0005
Formvar Solution in Ethylene Dichloride	Electron Microscopy Sciences	Cat. # 15810
Fura-IoAff K+ salt	Teflabs	Cat. #0137
Leupeptin	Sigma-Aldrich	Cat. #L8511-5mg
Li-Cor Blocking Buffer	Li-Cor	Cat. #927-50000
Diethyl malate	Sigma-Aldrich	Cat. #W237418
Mannitol	Thermo Fisher Scientific	Cat. #M120-3
MitoTracker Red CMXros	Invitrogene	Cat. #M7512
Pepstatin A	Sigma-Aldrich	Cat. #P5318-5mg
Percoll	Sigma-Aldrich	Cat. #P1644-100ml
Potassium hexacyanoferrate(II)-13C6 trihydrate	Sigma-Aldrich	Cat. # 736716
Resolving buffer	Biorad	Cat. #161-0798
Rhod - 2, AM	Anaspec	Cat. #AS84035
Ru360 - Calbiochem	Millipore Sigma	Cat. #557440
SlowFade Gold Antifade Mountant	Thermo Fisher Scientific	Cat. #S36937
Sodium Cacodylate Buffer, 0.2M, pH 7.4	Electron Microscopy Sciences	Cat. # 11652
Stacking buffer	Biorad	Cat. #161-0799
TEMED	Biorad	Cat. #161-0800
Thapsigargin	Enzo Life Sciences	Cat. #BML-PE180-0005
Tetramethylrhodamine, Methyl Ester, Perchlorate (TMRM)	Invitrogene	Cat. #T668
Uranyl Acetate	Electron Microscopy Sciences	Cat. # 22400

(*Continued on next page*)

Continued

REAGENT or RESOURCE	SOURCE	IDENTIFIER
Critical Commercial Assays		
DC protein assay kit	Biorad	Cat. #500-0114
Trans-blot turbo transfer kit	Biorad	Cat. #170-4271
Experimental Models: Cell Lines		
H9C2 cells	ATTC	Cat. #CRL-1446
Experimental Models: Organisms/Strains		
C57BL/6j mice	Jackson Laboratories	Cat. #000664
Male Sprague-Dawley rats	Envigo	Cat. #400
Slc8b1$^{fl/fl}$ x αMHC-MerCreMer mice	(Luongo et al., 2017)	N/A
αMHC-tTA x TRE-NCLX mice	(Luongo et al., 2017)	N/A
Recombinant DNA		
Human NCLX-FLAG/NCKX6-FLAG	(Cai and Lytton, 2004)	Addgene #75217
CEPIA3mt Ca^{2+} sensor	(Suzuki et al., 2014)	Addgene # 58219
Software and Algorithms		
ImageJ	NIH	https://fiji.sc/
Sigmaplot	SYSTAT	https://systatsoftware.com/products/sigmaplot/
Spectralyzer imaging and analysis software	MitoCare Center	N/A
Zen Black edition	Zeiss	https://www.zeiss.com/microscopy/int/downloads/zen.html

CONTACT FOR REAGENT AND RESOURCES SHARING

Further information and requests for resources and reagents should be directed to and will be fulfilled by the Lead Contact, Gyorgy Csordas (Gyorgy.csordas@jefferson.edu).

EXPERIMENTAL MODEL AND SUBJECT DETAILS

Mice and rats

All studies were done in accordance with the National Institutes of Health Guide for the Care and Use of Laboratory Animals, and the protocols were applied in compliance with the Thomas Jefferson University institutional animal care and use committee (IACUC) guidelines. Male Sprague-Dawley rats of 300–350 g (Envigo) and C57BL/6J mice of 25–30 g body weight (from Jackson Laboratories) were used to obtain heart homogenates. NCLX cKO and NCLX OE mouse models were generated as described earlier (Luongo et al., 2017).

Cell culture and DNA transfection

H9C2 cells were grown in Dulbecco's modified Eagle's medium supplemented with 10% fetal bovine serum,1% glutamine, 100 units/ml penicillin and 100 units/ml streptomycin. Cells were plated onto 25mm round coverslips and 24h later transfected with NCLX-FLAG (human NCKX6-FLAG (Cai and Lytton, 2004)) and/or CEPIA3mt (Suzuki et al., 2014), using 1μg of cDNA per ml of medium, following the manufacturer instructions (Lipofectamine 3000, Invitrogene). The NCLX OE was optimal after 48h of transfection.

METHOD DETAILS

Heart Mitochondria and jSR Isolation

Mice were euthanized by cervical dislocation, and the heart was immediately excised, washed, and placed in isolation buffer, containing 225 mM mannitol, 75 mM sucrose, 20 mM HEPES, 0.1 mM EGTA, and 1 g/liter BSA, pH 7.4. Of note, this isolation buffer lacks proteases in order to preserve protein tethering between mitochondria and jSR. After excising the heart, all steps were done on ice, and centrifuge steps were done at 4°C. Ventricular muscle tissue was carefully minced, rinsed, and then homogenized with a 5 mL glass-Teflon homogenizer (Wheaton) (20 up-down strokes at 300 rpm). Crude mitochondrial and SR fractions and rat cardiac muscle homogenates were prepared as described earlier (De La Fuente et al., 2016). Percoll purification of the mitochondrial fraction was

done as described previously (De La Fuente et al., 2016). Rats were euthanized by decapitation. The heart was immediately removed, and mitochondrial and jSR fractions were prepared as described earlier (De La Fuente et al., 2016).

$^{45}Ca^{2+}$ Retention Assays

Membrane fractions (250 μg/ml) were rapidly resuspended in 120 or 420μl of intracellular medium (120 mM KCl, 10 mM NaCl, 1 mM KH_2PO_4, 20 mM HEPES/Tris, 2 mM MgATP,) supplemented with protease inhibitors (leupeptin, antipain, and pepstatin; 1μg/ml each), thapsigargin (Tg; 2 μM), caffeine (10 mM), EGTA/Tris (pH 7.4) (50μM), and malate and pyruvate (1mM of each to energize mitochondria). Na^+-dependent mitochondrial Ca^{2+} extrusion was blocked by CGP (20μM) or Na^+ free intracellular medium. $^{45}Ca^{2+}$ uptake assays were performed as described previously (De La Fuente et al., 2016). For the $^{45}Ca^{2+}$ extrusion assays, 100-μl aliquots were collected just before Ru360 addition, and then after 30 s, 60 s and 3min. The Aliquots were rapidly diluted in 5 mL of ice-cold washing buffer (140 mM KCl, 10 mM HEPES/Tris, 0.5 mM EGTA/Tris, pH 7.2) and filtered through 0.3-μm nitrocellulose filters (Millipore). Filters were rinsed once with washing buffer, and $^{45}Ca^{2+}$ in the captured membrane particles was quantified by liquid scintillation counting. Sequestration data were corrected to citrate synthase activity as described earlier (De La Fuente et al., 2016).

Fluorescence wide field imaging

Prior to experiments, cells were loaded either with 100nM TMRM for 20 min or 2 μM Rhod-2 AM for 35 min both at 37°C in an extracellular medium (121 mM NaCl, 4.7 mM KCl, 1.2 mM KH_2PO_4, 1.2 mM $MgSO_4$, 2 mM $CaCl_2$, 5 mM $NaHCO_3$, 10 mM glucose, 10 mM HEPES, pH 7.4) supplemented with 2% (w/v) bovine serum albumin. After multiple washing steps with a Ca^{2+}-free extracellular buffer (120 mM NaCl, 20 mM Na–HEPES, 5 mM KCl, 1 mM KH_2PO_4, 100 μM EGTA/Tris pH 7.4) cells were permeabilized in intracellular medium supplemented with protease inhibitors, 2 mM MgATP, 40μg/ml saponin and 20μM EGTA/Tris (to chelate a small Ca^{2+} contamination in the saponin) for 5 min, @37°C on the thermostated stage of a Leica DMI6000 B microscope. In turn, for the recording the cells washed into fresh intracellular medium, supplemented with protease inhibitors, 2 mM MgATP, 2mM succinate/Tris and 1μM Fura-IoAff K+ salt. Fluorophores were excited by means of a Lambda DG-4 ultra-high-speed wavelength switcher light source (Sutter Instruments). The excitation filters (from Chroma) used were 340/10 nm, 380/10 nm for Fura, 550/15nm for Rhod-2 and 470/10nm for CEPIA3mt. Through an Olympus UApo/340 40x/1.35NA oil UV-optimized objective (fitted with an adaptor), the images of the emitted fluorescence were collected using a Fura/Rhod dichroic mirror (73100, EM 73101 Chroma Technology) or a Fura/Green/Red customized multi-band emission set (59022bs, 59055 m Chroma Technology) and recorded every 2 s by a ProEM 1024 EMCCD camera from Princeton Instruments. Single-cell records were analyzed with the custom-made software, Spectralyzer.

Protein Analysis and western blot

A biuret-based reagent kit from Bio-Rad (DC protein assay kit) was used to measure the protein concentrations for the isolated mitochondria and jSR. Western blot was done using a Bio-Rad setup, including a Trans-Blot®Turbo transfer system. Equal amounts of total protein were loaded, separated electrophoretically by SDS-PAGE (12%–15% gels), and transferred to a nitrocellulose membrane. After a blocking step in LI-COR Odyssey blocking solution (1 h at room temperature), the membrane was incubated overnight at 4°C with primary antibodies. The LI-COR infrared fluorescent secondary antibodies (IRDye 800CW) were used for visualization by means of a LI-COR Odyssey scanner. Band quantification (“densitometry”) was performed using ImageJ software (National Institutes of Health). Owing to the different distribution of proteins among the fractions, we could not use a “housekeeping” protein as traditional loading control reference.

Fluorometric Measurements of $[Ca^{2+}]_o$

Experiments were performed as described in (Paillard et al., 2017) but without the NCLX inhibitor CGP-37157. Isolated mitochondria (750μg of protein/ml) were resuspended in 1.5 ml intracellular medium in a stirred thermostated (35°C) plastic cuvette. $[Ca^{2+}]o$ was monitored using fura-2 LoAff (1.5μM) in the intracellular medium by means of a multiwavelength excitation dual wavelength emission fluorimeter (DeltaRAM, Horiba/PTI) at 340- and 380-nm excitation and 500-nm emission at 20 points/s acquisition rate. $CaCl_2$ bolus was added using a Hamilton syringe via an addition port without pausing the data acquisition. Calibration of the Ca^{2+} signals was carried out at the end of the measurements with the addition of 1mM $CaCl_2$ and 10mM EGTA.

Immunofluorescence of H9C2 Cells

H9C2 cells plated and transfected as specified above, were loaded with MitoTracker®Red CMXRos (MtTrRed; 50 nM) during 20 min at 37°C, then fixed with 40 g/liter paraformaldehyde/PBS for 15 min. Fixed cells were subjected to a standard immunofluorescence staining protocol. 3% Bovine Serum Albumin and 0.2% Triton X-100 in PBS were used for blocking and permeabilization. Secondary antibodies were conjugated with Alexa Fluor®488 or 647 (to minimize spectral overlap with MtTrRed that is excited at 568 nm). To assess nonspecific binding of secondary antibodies, negative controls without primary antibody were used. SlowFade® was used for mounting on microscope slides. Immunofluorescence was imaged using a Zeiss LSM880MP confocal microscope equipped with the Airyscan super-resolution (× 1.7 beyond the diffraction limit) detection system. A Zeiss 63x/ 1.4 NA oil plan-apochromat differential interference contrast objective was used to obtain all images. Image post-processing was done using Zen software from Zeiss and the Canvas X vectographic software.

TEM

Hearts were subjected to perfusion fixation. Mice were anaesthetized with intraperitoneal injection of Nembutal (90 mg/kg in PBS) and heparin (anticoagulant, 50 IU). The heart was excised from the chest cavity, cannulated and secured on a Langendorff apparatus for 5 minutes in Tyrode solution (in mM: 135 NaCl;, 5.4 KCl, 5 $MgCl_2x6H_2O$, 10 HEPES, 0.33 NaH_2PO_4, pH 7.4) supplemented with 1 mM $CaCl_2$ and then for 3 minutes in Tyrode solution supplemented with 3 μM $CaCl_2$. This was followed by 5 min perfusion with fixative solution (2.5% glutaraldehyde in 0.1 M Na-cacodylate buffer, pH 7.4) for 5 min, after which the whole heart was immersed in fixative for an additional 1 hour at room temperature. In turn, small pieces of left ventricular wall and papillary muscle (1-2 mm^3) are excised and fixed with 2.5% glutaraldehyde for another 30 min, after which they are post-fixed overnight in 2% osmium tetroxide partially reduced by 0.8% $K_4Fe(CN)_6$ in 0.15 M Na-cacodylate buffer. Samples were contrasted en bloc with 1% uranylacetate in diH_2O, dehydrated in graded series of acetone, embedded in Spurr's resin per manufacturer's instructions. Longitudinal, ultrathin sections (65-80 nm) were cut from the resin-embedded blocks with a diamond knife (Diatome-US, USA) using a Leica UCT ultramicrotome and caught on copper grid covered with formvar film. Images of longitudinal oriented cardiomyocytes were obtained via an FEI Tecnai 12 TEM fitted with an AMT XR-111 10.5 Mpx CCD camera at 3,200 - 15,000x magnification (80 kV). Morphometric analysis of mitochondria and the jSR-mitochondrial associations was performed using ImageJ (NIH). To get the general information about mitochondrial morphology and abundance (the area of mitochondria and perimeter), a mask was drawn over the sarcoplasmic area in cardiomyocyte longitudinal sections. The percent of the sarcoplasmic area covered by mitochondria was used for determination of mitochondrial volume density. For the morphometric analysis of SR-mitochondrial associations a custom plugin was used (created by David Weaver). Mitochondria which were in association with jSR in their transversal side (at the Z-line) were analyzed. Mask of mitochondria, the transversal side (line segment) of outer mitochondrial membrane and the interfacing jSR membrane line (in distance < 50 nm) were created. Mean gap distance, length of transversal side of mitochondria, length of jSR and of the interface (mitochondria outer membrane-jSR) values were generated by the plugin.

QUANTIFICATION AND STATISTICAL ANALYSIS

Statistical analysis was performed using the Sigmaplot software. Raw data from each individual experiment was evaluated using a two-tailed t test (or rank sum test for TEM analysis) with 95% confidence in Sigmaplot. Further details are provided within the corresponding figure legend.